Optimal Path Planning for Robotic Insertion of Steerable Electrode Arrays in Cochlear Implant Surgery

Jian Zhang
Department of Mechanical Engineering,
Columbia University,
New York, NY 10027

J. Thomas Roland, Jr.
Department of Otolaryngology and Neurosurgery,
New York University Medical Center,
New York, NY 10016

Spiros Manolidis
Department of Head & Neck Surgery,
Beth Israel Hospital,
New York, NY 10003

Nabil Simaan[1]
Department of Mechanical Engineering,
Columbia University,
New York, NY 10027

This paper presents an optimal path planning method of steerable electrode arrays for robot-assisted cochlear implant surgery. In this paper, the authors present a novel design of steerable electrode arrays that can actively bend at the tip. An embedded strand in the electrode array provides an active steering degrees-of-freedom (DoF). This paper addresses the calibration of the steerable electrode array and the optimal path planning for inserting it into planar and three-dimensional scala tympani models. The goal of the path planning is to minimize the intracochlear forces that the electrode array applies on the walls of the scala tympani during insertion. This problem is solved by designing insertion path planning algorithms that provide best fit between the shape of the electrode array and the curved scala tympani during insertion. Optimality measures that account for shape discrepancies between the steerable electrode array and the scala tympani are used to solve for the optimal path planning of the robot. Different arrangements of DoF and insertion speed force feedback (ISFF) are simulated and experimentally validated in this paper. A quality of insertion metric describing the gap between the steerable electrode array and the scala tympani model is presented and its correspondence to the insertion force is shown. The results of using 1DoF, 2DoF, and 4DoF electrode array insertion setups are compared. The 1DoF insertion setup uses nonsteerable electrode arrays. The 2DoF insertion setup uses single axis insertion with steerable electrode arrays. The 4DoF insertion setup allows full control of the insertion depth and the approach angle of the electrode with respect to the cochlea while using steerable electrode arrays. It is shown that using steerable electrode arrays significantly reduces the maximal insertion force (59.6% or more) and effectively prevents buckling of the electrode array. The 4DoF insertion setup further reduces the maximal electrode insertion forces. The results of using ISFF for steerable electrodes show a slight decrease in the insertion forces in contrast to a slight increase for nonsteerable electrodes. These results show that further research is required in order to determine the optimal ISFF control law and its effectiveness in reducing electrode insertion forces. [DOI: 10.1115/1.3039513]

Keywords: surgical assistance, cochlear implant, path planning, underactuated robot, steerable electrode array

1 Introduction

The problem of inserting flexible underactuated objects into human anatomies is important for safe catheter insertion [1], neurosurgery [2], endovascular surgery [3], colonoscopy [4], etc. This paper focuses on the kinematics, calibration, and optimal path planning for safe insertion of steerable electrode array (Fig. 1(*a*)) into a given 3D cavity (scala tympani inside the cochlea) (Fig. 1(*b*)). The motivation behind this work is the need for a mechanism of safe electrode array insertions in cochlear implant surgery. The underactuated steerable electrode array in Fig. 1(*a*) assumes a predetermined 3D minimal energy shape when actuated [5]. The calibration of the steerable electrode array and the optimal path planning for safe insertion are presented in this paper. An optimal insertion minimizes the required insertion force of the electrode array. This optimality criterion is used because increased insertion forces are directly related to the increased risk of buckling of the electrode array inside the scala tympani and therefore increased trauma to surrounding anatomies.

Due to the small size of the steerable electrode array, we assume that controlling its shape is limited by using a single actuator. The importance of three additional degrees-of-freedom (DoFs) required for the steerable electrode array is evaluated through simulations and experiments. We compare the insertions using 1DoF system (Fig. 1(*c*)), 2DoF system (Fig. 1(*d*)), and 4DoF system (Fig. 1(*e*)), respectively. This paper proposes the simulated average angle and distance variations as an optimality measure and correlates it to the shape similarity between the steerable electrode array and the scala tympani.

Previous works on flexible object insertions focused mainly on inserting flexible beams into straight holes [6], modeling and path planning for flexible object manipulation [6–11], and robot-assisted insertion of steerable catheters [1]. Among all previous works, the most relevant ones to our problem are [5,6,9] on flexible beam insertion into a straight hole.

Zheng et al. [6] assumed a modal representation of a flexible beam based on the work of Rohde [7]. The deflection of the beam was depicted by applying large deflection theory in uniformly distributed load. Their paper addressed two cases: insertion with loose tolerance and insertion with a tight tolerance. It was found that the robot gripper only needs to follow the shape of a deflected beam during the insertion for the loose clearance case. The tight-

[1]Corresponding author.

Manuscript received April 4, 2008; final manuscript received October 21, 2008; published online December 18, 2008. Review conducted by M. Y. Lee.

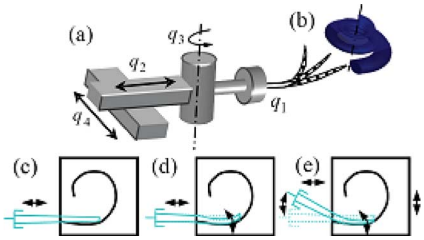

Fig. 1 Problems with different DoF arrangements considered: (*a*) underactuated robot, (*b*) known 3D helical cavity, (*c*) 1DoF insertions, (*d*) 2DoF insertions, and (*e*) 4DoF insertions

clearance case required modifying the position of the robot gripper along the involute of the beam curve prior to reattempting insertion by following the deflected beam curve.

The simplified approach of Zheng et al. [6] is based on a closed-form series approximation of the deformation shape of the beam and is useful for real-time control, but it is limited and cannot deal with interactions between the beam and obstacles. Nakagaki et al. [12] used a similar approach but provided a method of inserting by varying the orientation of the beam end if the friction is large enough to cause beam buckling. They also implemented vision-guided insertion [8]. Despite these works, the problem of safe insertion of a flexible object into a 3D cavity has not been addressed. Our work differentiates itself from these previous works since it addresses the problem of safe insertion of a flexible underactuated object into a curved cavity instead of a simple hole.

The main contributions of this paper include a general path planning algorithm for inserting underactuated steerable electrode array into a curved cavity (scala tympani). The clinical motivation of our approach is explained with its relevance to cochlear implant surgery. The importance of changing the end conditions of the flexible object as opposed to only controlling its steerable portion is compared by simulation and verified by experiments. A physically meaningful optimality measure is defined and correlated with the required insertion forces obtained from the experimental results.

Section 2 of this paper describes the clinical motivation of our research. The kinematic modeling of a robotic system inserting a steerable electrode array and its calibration are provided in Sec. 3. Section 4 applies the modal approach [13–15] to determine the shape of the steerable electrode array and solves for the insertion path planning of the steerable electrode array. Section 5 presents the calibration and simulations of the insertion process and comparison between systems with different DoF. Finally, Sec. 6 presents the experimental setup and experimental results using 1DoF, 2DoF, and 4DoF systems. A comparison of the insertions into planar and 3D cavity models (scala tympani) with and without ISFF is also addressed in this section. The explanation for the effectiveness of the path planning algorithm of the flexible robot follows in the end.

2 Clinical Motivation

Cochlear implant surgery restores partial hearing for patients suffering from severe hearing loss due to damaged or dysfunctional neuroepithelial (hair) cells in the inner ear. The cochlear implant system includes a microphone, a signal processor, a transmitter, a receiver, and an electrode array, see Fig. 2. This system converts the sound waves into electrical signals that are delivered to the auditory nerve through the implanted electrode array. The electrode array is implanted inside the scala tympani, see Fig. 2 (though some earlier works explored insertion into the scala vestibuli [16]).

The application of cochlear implants to patients with residual hearing is limited by the design technology and insertion techniques of existing electrode arrays. Current electrode arrays are

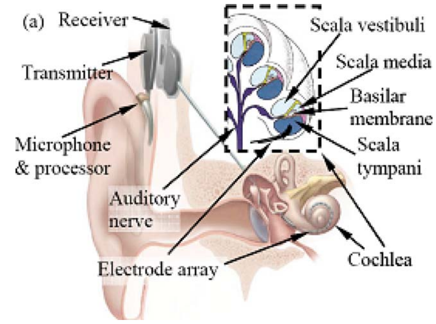

Fig. 2 Cochlear implant system components and cochlear anatomy

straight or precurved [17]. They have various lengths, thicknesses, and flexibilities. The interaction forces with scala tympani during surgery are small, usually less than 10 g. But the tools used by surgeons provide very limited force feedback. Because the fine anatomy of the scala tympani does not lend itself to intraoperative imaging during cochlear implant surgery, the delicate structures of the scala tympani can be easily ruptured by the inserted electrode array. All these characteristics of cochlear implant surgery currently limit both its success and applicability in expanded patient population.

Previous studies on the properties and designs of electrode arrays focused on characterizing their stiffness [18], buckling limits [18,19], and insertion contact pressure against the walls of the cochlea [17,20]. Kha et al. [18] determined stiffness properties of electrode arrays based on three-point flexural bending and buckling tests.

Roland [17] compared the designs and insertion methods of the contour electrode array with the Contour Advance electrode array by Cochlear Corp. With the lack of real-time imaging, the increase in insertion forces and the trauma to the cochlea are inevitable, as was shown in the trauma studies by Wardrop et al. [21]. Other trauma studies [22–24] compared different designs of electrode arrays and obtained low success rates of atraumatic insertions. Considering any kind of trauma, the average atraumatic rates in Refs. [21–24] vary from 34% to 62%. In some cases [24], the atraumatic rate can be as low as 0–20%.

In Ref. [5], a new design of actively bent steerable electrode arrays was conducted. These steerable electrode arrays were actuated using an actuation wire embedded in a silicone rubber electrode array. Subsequently Chen et al. [25] used nitinol shape memory alloy wires embedded inside the electrode array to provide steerability. Also, there are groups working on designing miniature sensors for position and tip contact to minimize insertion damage and optimize implant placement [26].

The assumption made in this paper is that the decrease in the insertion force of the electrode array will significantly reduce its buckling risk and the trauma rate during cochlear implant surgery. This assumption is used to define the optimal insertion path planning and to experimentally compare between different insertion strategies.

3 Kinematic Modeling

3.1 Steerable Electrode Arrays. Figure 3 shows the conceptual design of the steerable electrode array for cochlear implant surgery [5]. Different from the commercial electrode arrays, it has a Kevlar strand embedded inside. The strand is offset from the center of the electrode array and it is fixed at its tip, see Fig. 3(*b*). When the strand is pulled at the base, different bent shapes are obtained [5]. Considering the fabrication cost to make a real electrode, we first fabricated a 3:1 scaled up steerable electrode array based on MedEl electrode.

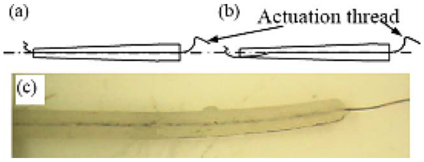

Fig. 3 Steerable electrode array: (*a*) side view, (*b*) top view, and (*c*) physical model

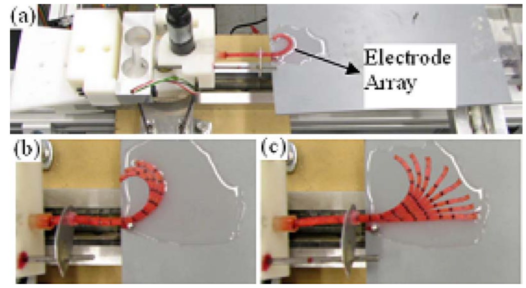

Fig. 4 (*a*) Electrode calibration setup, (*b*) shallow insertion depth with supporting ring position, and (*c*) deep insertion depth with supporting ring position

3.2 Scala Tympani Model. The 2D template of the scala tympani model was first provided by Cohen et al. [27] to aid surgeons with an estimation of the insertion angle. Based on their model, a scaled up (3:1) planar scala tympani model is made [5]. This model provides an insertion angle up to 340 deg, which is enough to demonstrate the effectiveness of using steerable electrode arrays because buckling in the unactuated case can be avoided with active steering.

Three-dimensional modeling of the scala tympani was addressed by Yoo et al. [28] who presented an internet-based 3D visualization tool for the cochlea based on a 3D generalization of the 2D spiral template of Cohen et al. and the data from Ketten et al. [29]. The backbone curve of the scala tympani is given by Eq. (1) where r, z, and θ are the cylindrical coordinates of this curve (r is the radial distance to the curve, z is the height, and θ is the angle). The values of the constants a, b, c, d, θ_0, and p are based on Yoo et al. [28]. This 3D scala tympani model has a fixed angle helix, which leads to a simple solution of the insertion angle. The cross section of the scala tympani is modeled by an ellipse according to dimensions from Wysocki's work [30].

$$R = \begin{Bmatrix} c(1 - d\log(\theta - \theta_0)), & \theta < 100 \text{ deg} \\ ae^{-b\theta}, & \theta \geq 100 \text{ deg} \end{Bmatrix}, \quad z = p(\theta - \theta_0)$$
$$\theta \in [10.3 \text{ deg}, 910 \text{ deg}], \tag{1}$$

3.3 Kinematics of Steerable Electrode Arrays. The shape of the planar bent electrode array is characterized by $\theta_e(s,q_1)$, where θ_e is the angle at arclength s along the backbone of the electrode array given the actuation of the strand q_1. $s=0$ represents the base of the electrode array and $s=L$ denotes the tip of the electrode array. Let the minimal energy solution for the direct kinematics of the electrode array be approximated using a modal representation in Eq. (2), where $\mathbf{a}$ is the vector of modal factors.

$$\theta_e(s,q_1) = \boldsymbol{\psi}(s)^T \mathbf{a}(q_1), \quad \mathbf{a}, \boldsymbol{\psi} \in \Re^n \tag{2}$$

where $\boldsymbol{\psi}(s) = [1, s, s^2, \ldots, s^{n-1}]^T$. Further denote the modal factors by

$$\mathbf{a}(q_1) = \mathbf{A}\,\boldsymbol{\eta}(q_1) \tag{3}$$

where $\boldsymbol{\eta} \in \Re^m$, $\mathbf{A} \in \Re^{n\times m}$, and $\boldsymbol{\eta} = [1, q_1, q_1^2, \ldots, q_1^{m-1}]^T$. For high-order polynomial approximations ($m > 6$), a set of orthogonal polynomials (e.g., Chebyshev polynomials) should be used for considerations of numerical stability [31]. Through experimental digitization, the shape of the electrode array is digitized by r equidistant points along its backbone in z different images of the electrode array associated with z different values of q_1 (the amount of pull on the actuation strand). The digitization results are stored in the experimental data matrix $\boldsymbol{\Phi} \in \Re^{r\times z}$, where $\boldsymbol{\Phi}_{i,j} = \theta_e(s_i, q_{1j})$. Using the modal representation in Eq. (2), the experimental data matrix is expressed by Eq. (4).

$$\boldsymbol{\Phi} = \underbrace{\begin{bmatrix} \boldsymbol{\psi}^T(s=0) \\ \vdots \\ \boldsymbol{\psi}^T(s=s_{\max}) \end{bmatrix}}_{\boldsymbol{\Omega}} \mathbf{A}_{n\times m} \underbrace{\left[\boldsymbol{\eta}(q_1=0), \quad \ldots, \quad \boldsymbol{\eta}(q_1=q_{1\,\max}) \right]}_{\boldsymbol{\Gamma}}$$
$$= \boldsymbol{\Omega}_{r\times n} \mathbf{A}_{n\times m} \boldsymbol{\Gamma}_{m\times z} \tag{4}$$

where

$$\boldsymbol{\Omega} = \begin{bmatrix} 1 & s=0 & \cdots & s=0^{n-1} \\ & & \vdots & \\ 1 & s=s_{\max} & \cdots & s=s_{\max}^{n-1} \end{bmatrix}_{r\times n}$$

and

$$\boldsymbol{\Gamma} = \begin{bmatrix} 1 & & 1 \\ q_1 & \cdots & q_{1\,\max} \\ \vdots & & \vdots \\ q_1^{m-1} & & q_{1\,\max}^{m-1} \end{bmatrix}_{m\times z}$$

are Vandermonde matrices corresponding to the r numerical values of s and the z values of q_1 used to generate the experimental data matrix $\boldsymbol{\Phi}$. Solving Eq. (4) for the electrode array calibration matrix $\mathbf{A}$ provides the required solution for the direct kinematics problem. The solution of this algebraic matrix equation is given by $[\boldsymbol{\Gamma}^T \otimes \boldsymbol{\Omega}]\mathrm{Vec}(\mathbf{A}) = \mathrm{Vec}(\boldsymbol{\Phi})$, where $\otimes$ represents Kronecker's matrix product [32] and $\mathrm{Vec}(\mathbf{A}_{m\times n}) = [a_{11} \cdots a_{m1}, a_{12} \cdots a_{m2}, \ldots, a_{1n} \cdots a_{mn}]^T$.

3.4 Electrode Array Calibration. As described in Sec. 3.3, the shape characteristics of the electrode array are fully expressed by the calibration matrix $\mathbf{A}$, which is solved experimentally. The calibration setup of the electrode array is shown in Fig. 4(*a*). In the calibration process, only the joint for pulling the actuation strand of the electrode array is active. The electrode is placed on a platform with glycerin in between to reduce the friction between the electrode and the supporting platform.

Since the electrode array is long and subject to buckling, a support ring is needed to prevent this failure mode at the unsupported portion of the electrode array outside the scala tympani model. Although the position of the support ring can be continuously changed during the insertion, we chose to place the ring in an extended position during shallow insertions and in a retracted position during deep insertions, see Figs. 4(*b*) and 4(*c*). In each picture, the bending angles at each marking point are recorded. Then the experimental data matrix $\boldsymbol{\Phi}$ is calculated from the calibration figures, yielding the calibration matrix $\mathbf{A}$ by the algebraic matrix equation (Eq. (4)).

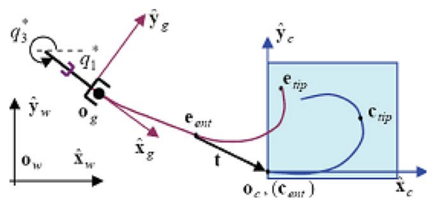

Fig. 5 Angle and offset optimization of the underactuated robot

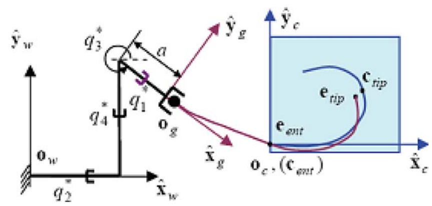

Fig. 6 Inverse kinematics of the underactuated robot

4 Optimal Path Planning for Robotic Electrode Insertion

4.1 Objective of Optimization. An optimization algorithm is applied to solve for the shape, orientation, and position of the inserted and bent part of the electrode array such that it can best approximate the curved shape of the scala tympani. This assumption is meaningful in the sense that when the shape of the bent electrode array matches the curve of the scala tympani, the insertion will be proceed with less force than a geometrically unmatched array. In order to find the best shape at each insertion depth, the optimization problem is solved by finding the optimal paths for the steerable electrode array and all three additional DoF of the insertion unit. Once these optimal paths are found, this optimization problem is solved.

The anatomical 3D scala tympani model based on Eq. (1) has a constant helix angle. Since the steerable electrode array used in the experimental setup is designed to bend in plane, it is tilted about its longitudinal axis by an angle equal to the helix angle of the scala tympani. This simplifies the insertion path planning and the electrode array design and fabrication. Hence, the optimal insertion path planning is achieved based on the planar scala tympani model [27].

4.2 Optimal Insertion Path Planning. The problem of insertion path planning includes finding the optimal orientation and position of the base of the electrode array and the optimal steering of its tip in order to minimize intracochlear damage during insertion. Figure 1(*a*) shows the kinematic layout of a 4DoF robot comprised of an insertion unit and a steerable underactuated electrode array. The insertion unit is a 3DoF planar robot that allows adjusting the angle and the offset of the electrode array with respect to the scala tympani.

Figure 5 shows an electrode array that is optimally bent and rotated in plane in order to fit the shape of the scala tympani for a given insertion depth. Frames $\{w\}$, $\{g\}$, and $\{c\}$ designate the world coordinate system, the robot gripper coordinate system, and the cochlea coordinate system. q_1^* designates the optimal amount of retraction of the actuation strand of the steerable electrode array. q_3^* denotes the optimal rotation of the robot gripper. $\mathbf{c}_{\text{tip}}$ is the point on the centerline of the scala tympani that corresponds to the tip of the inserted electrode array $\mathbf{e}_{\text{tip}}$. $\mathbf{e}_{\text{ent}}$ is the point on the centerline of the electrode array that corresponds to the entrance of the scala tympani $\mathbf{c}_{\text{ent}}$.

4.2.1 Orientation Optimization. Once the electrode array calibration matrix $\mathbf{A}$ is generated, for any given q_1, $\tilde{\boldsymbol{\theta}}_e(s)$ yields a column vector of $\boldsymbol{\Phi}(s,q_1)$ that represents the shape of the bent electrode array. Similarly, the shape of the scala tympani can be defined as $\tilde{\boldsymbol{\theta}}_c(s_c)$, where $s_c \in [0,L_c]$ is the arclength along the central curve of the scala tympani model. The insertion depth d is defined by the arclength of the inserted part of the electrode array. The objective function for angle optimization is given by Eq. (5).

$$\underset{q_1^*,q_3^*}{\operatorname{argmin}} \tfrac{1}{2}\mathbf{T}^T\mathbf{W}(d)\mathbf{T} \tag{5}$$

where

$$\mathbf{T} = [\mathbf{S}_c(d)\tilde{\boldsymbol{\theta}}_c - (\mathbf{S}_e(d)\tilde{\boldsymbol{\theta}}_e(q_1) + \mathbf{q}_3(d))]$$

and

$$\underset{x}{\operatorname{argmin}}\, f(x) \in \{x \mid \forall\, y{:}f(y) \geq f(x)\}$$

denotes the value of x that minimizes $f(x)$. At insertion depth d, $\mathbf{S}_e(d)=\left[\begin{smallmatrix}\mathbf{0}_{L-d}\\ \mathbf{I}_d\end{smallmatrix}\right]$, where $\mathbf{I}_d$ represents the inserted part of the electrode array inside the scala tympani and $\mathbf{0}_{L-d}$ is the uninserted part of the electrode array. $\mathbf{S}_c(d)=\left[\begin{smallmatrix}\mathbf{I}_d\\ \mathbf{0}_{L-d}\end{smallmatrix}\right]$ denotes the length from the entrance $\mathbf{c}_{\text{ent}}$ of the scala tympani to the point where the electrode array tip $\mathbf{c}_{\text{tip}}$ reaches is d. $\mathbf{W}(d)$ is a weight matrix that specifies different weights to the steerable electrode array, from the tip to the base part. By varying these weights in the path planning, we can decide which portion of the electrode array simulates the curve of the scala tympani better. For any given insertion depth d, the optimal bending of the electrode array q_1^* and the optimal robot base rotation q_3^* are found. In this case, the angle differences between the inserted part of the electrode array and the scala tympani model are the smallest.

4.2.2 Position Optimization and Inverse Kinematics of the Insertion Unit. For any given insertion depth d, when the orientation is optimized, the position of the electrode array with respect to the scala tympani is constrained by the entrance of the scala tympani $\mathbf{c}_{\text{ent}}$. To achieve position optimality, Fig. 5, the offset $\mathbf{t}$ is given by

$$\mathbf{t}(d,q_1^*,q_3^*) = \mathbf{c}_{\text{ent}} - \mathbf{e}_{\text{ent}}(d,q_1^*,q_3^*) \tag{6}$$

Therefore, the optimized result of the electrode array position and orientation is given by

$$\mathbf{p}_e^*(s,q_1^*,q_3^*) = \mathbf{p}_c(s-(L-d)) + \mathbf{t}(d,q_1^*,q_3^*) \tag{7}$$

where $\mathbf{p}_c(s)$ represents the point of the scala tympani at arclength s in $\{w\}$, $\mathbf{p}_e^*(s,q_1^*,q_3^*)$ represents the point of the electrode array at arclength s in $\{w\}$, and $L-d \leq s \leq L$. The optimized result is shown in Fig. 6 where the inserted portion of the electrode approximates its corresponding curve of the scala tympani in the best way possible while respecting the constraint of the entrance point to the scala tympani. From the optimized results, Fig. 6 shows the position of the robot gripper, see Eq. (8).

$$\mathbf{o}_g^*(q_1^*,q_3^*) = \mathbf{p}_e^*(L-d,q_1^*,q_3^*) \tag{8}$$

The inverse kinematics of the robot can be easily solved in Fig. 6.

5 Calibration and Simulation Results

5.1 Calibration Results. In the calibration process, we digitized 13 marked points ($r=13$) on the steerable electrode array and took a series of 12 images ($z=12$) to get the experimental data matrix $\boldsymbol{\Phi}$, which is a 13×12 matrix. By solving Eq. (4), the solution of the calibration matrix is

$$\mathbf{A} = \begin{bmatrix} 7.905 \times 10^{-6} & -1.229 \times 10^{-5} & -3.819 \times 10^{-4} & 4.754 \times 10^{-4} \\ -1.162 \times 10^{-3} & 1.057 \times 10^{-2} & 5.942 \times 10^{-3} & -2.576 \times 10^{-2} \\ 2.653 \times 10^{-2} & -2.555 \times 10^{-1} & 2.532 \times 10^{-1} & 4.403 \times 10^{-1} \\ -1.285 \times 10^{-1} & 1.160 & -1.645 & -1.839 \end{bmatrix} \tag{9}$$

Before simulating the process of the electrode array insertion, we plotted different bent shapes of the electrode array with the same values of q_1 used in the calibration process. Figure 7 shows the shapes of the electrode throughout its full range of motion. The shapes of the electrode array in Fig. 7 correspond well with the calibration images shown in Fig. 4.

5.2 Numerical Path Planning Optimization Results. Given the calibration matrix **A** as in Eq. (9), the path planning optimization was solved by applying the objective function, see Eq. (5). We started searching for the optimal value of the objective function from insertion depth $d=10$ mm to $d=55$ mm with increments of 1 mm. Correspondingly, the range of rotation angle q_3 was restricted in $(-20\text{ deg}, 20\text{ deg})$ with increments of 1 deg. The pull of the actuation strand for optimal q_1 was calculated from 0 mm to 8.5 mm with a coarse increment of 0.7 mm. Once the most appropriate value was found, we searched for a more accurate value with fine increments (1/20 of coarse increments) within two nearby optimal values. The optimized results for bending of the electrode array q_1^* and the base rotation angle q_3^* are shown in Fig. 8(*a*). Continuous solid line shows the results of a fourth-order polynomial fitting of the optimized q_1^* (discrete cross points). Equation (10) gives the resulting polynomial with its coefficients. A single-parametric cubic spline (dashed line) was applied to approximate the optimized q_3^* (discrete dots). A number of u segments ($u=15$) were picked along the curve, and the segment break points are defined for insertion depth values given by $\mathbf{d} = [10,11,12,13,15,16,20,24,27,31,34,37,42,47,50,55]$. Each segment takes the form of Eq. (11).

For any spline segment j, the coefficients $b_{j,i}(i=1,2,3,4)$ are given by Eq. (12) [33]. Using the chord approximation, all the tangent vectors are solved by Eq. (13) where $\mathbf{q}_3' = [q_{3,1}', q_{3,2}', \ldots, q_{3,u}']^T$ and matrices **M** and **R** are given by Eqs. (14) and (15).

$$q_1^*(d) = a_4 \times d^4 + a_3 \times d^3 + a_2 \times d^2 + a_1 \times d + a_0,$$

$$a_4 = 9.6345 \times 10^{-7}, \quad a_3 = -8.7915 \times 10^{-5},$$

$$a_2 = 8.7275 \times 10^{-4}, \quad a_1 = 2.3942, \quad a_0 = -1.3966 \tag{10}$$

$$q_3(d) = \sum_{i=1}^{4} b_{j,i} d^{i-1}, \quad d_j < d < d_{j+1} \quad \text{for segment } j,$$

$$j = 1, 2, \ldots, u \tag{11}$$

$$\mathbf{b}_j = \begin{bmatrix} b_{j,1} \\ b_{j,2} \\ b_{j,3} \\ b_{j,4} \end{bmatrix} = \begin{bmatrix} 1 & 0 & 0 & 0 \\ 0 & 1 & 0 & 0 \\ -3/d_{j+1}^2 & -2/d_{j+1} & 3/d_{j+1}^2 & -1/d_{j+1} \\ 2/d_{j+1}^3 & 1/d_{j+1}^2 & -2/d_{j+1}^3 & 1/d_{j+1}^2 \end{bmatrix} \begin{bmatrix} q_{3,j} \\ q_{3,j}' \\ q_{3,j+1} \\ q_{3,j+1}' \end{bmatrix} \tag{12}$$

$$\mathbf{q}_3' = \mathbf{M}^{-1}\mathbf{R} \tag{13}$$

$$\mathbf{M} = \begin{cases} m_{j-1,j} = d_{j+1}, \quad m_{j,j} = 2 \times (d_j + d_{j+1}), m_{j+1,j} = d_j & \text{for } 2 \le j \le u-1 \\ m_{1,1} = m_{u,u} = 1 & \\ m_{i,j} = 0 & \text{elsewhere} \end{cases} \tag{14}$$

$$\mathbf{R} = \begin{cases} r_{j,1} = \dfrac{3}{d_j d_{j+1}}(d_j^2(d_{j+1} - d_j) + d_{j+1}^2(d_j - d_{j-1})) & \text{for } 2 \le j \le u-1 \\ r_{j,1} = q_{3,j}' & \text{for } j=1 \text{ or } j=u \end{cases} \tag{15}$$

By solving the inverse kinematics using the optimization results, discrete end effector positions (discrete dots) are plotted in Fig. 9. Figure 9 shows the required motion of the gripper for optimal insertion of the steerable electrode array. Figure 8(*b*) shows the optimized values for q_2^* (discrete dots) and q_4^* (discrete circles) based on Eqs. (11)–(13). These values give the optimal translation of the gripper that matches the path in Fig. 9. The paths for the prismatic joints after cubic spline interpolation (solid and dashed lines) are also shown in Fig. 8(*b*).

5.3 Simulation Results. Figure 10 demonstrates the effectiveness of the insertion path planning based on the results of Sec. 5.2. The figure shows that the optimal position and orientation of the electrode were successfully found in order to optimally fit the shape of the scala tympani.

Figure 8 provided the optimal rotation and translation of the electrode base. This requires a 4DoF electrode insertion setup as in Fig. 13. We compare this 4DoF setup with a simpler 2DoF setup [5], in which the orientation of the electrode base is constant and the translation of the electrode base is only in the insertion direction while the electrode is steerable.

A simulation of the insertion process for the 2DoF and the 4DoF setup is shown in Fig. 11. The figure clearly shows that the 4DoF system provides a better shape fit between the electrode and the scala tympani curve when compared with the 2DoF system. To quantify the shape difference between the bent electrode array and the scala tympani curve, the simulated average angle and distance variations were defined as in Eqs. (16) and (17).

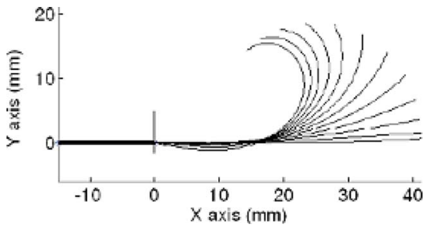

Fig. 7 Simulation results of bent electrodes

$$\bar{\theta} = \frac{1}{d}\int_0^d |\theta_c(s) - \theta_e(L-d+s)|ds \tag{16}$$

$$\bar{p} = \frac{1}{d}\int_0^d \|\mathbf{p}_c(s) - \mathbf{p}_e(L-d+s)\|ds \tag{17}$$

The average angle and distance variations provide quantitative measures that describe the shape discrepancies between the bent electrode array and the scala tympani model. Small values of these average variations give a better shape fit between the electrode array and the scala tympani. Hence, the insertion force will be smaller due to the small shape discrepancies.

As seen from Fig. 12, during the insertion process, the 4DoF system keeps smaller angle and distance variations than the 2DoF system. These results agree with the visual inspection of Fig. 11. This provides a justification for using a 4DoF system in which the steerable tip of the electrode is controlled as well as the 3DoF position and orientation of its base.

6 Experimental Setup and Results

6.1 Experimental Setup. Figure 13 shows the experimental setup used to validate the insertion path planning. It uses scaled up (3:1) models of the scala tympani. The setup using a 3D model of the scala tympani is shown. The plane in which the electrode bends is tilted at a certain angle to match the helix angle of the scala tympani model. A scaled up (3:1) model of a typical electrode array was fabricated using silicone rubber. An AG NTEP 5000d single axis force sensor was used in the setup to measure the axial insertion force of the electrode array and it was capable of detecting ± 0.1 g force using a 13 bit A/D acquisition card. The robot position control was achieved using Linux Real Time Application Interface (RTAI) with a closed loop rate of 1 kHz.

With each setup, insertions using 1DoF (nonsteerable electrode

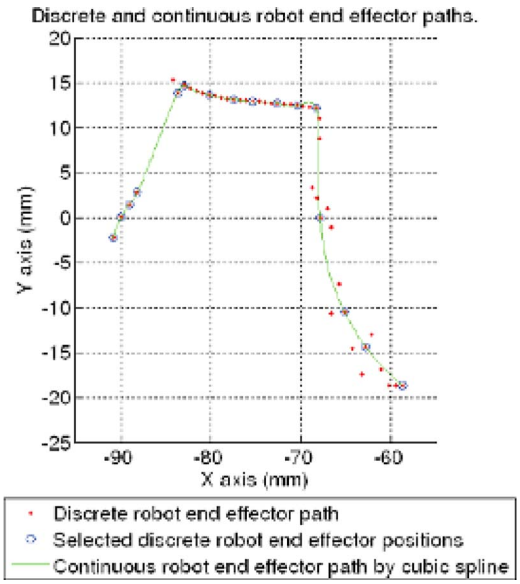

Fig. 9 Spline results of end effector path for the underactuated robot

array), 2DoF, and 4DoF experimental systems (using steerable electrode array) were carried out. For 1DoF insertions, only the actuation unit q_2 is activated. 2DoF insertions use both joints q_1 and q_2 so that the electrode array is steered according to the predefined path. For the 4DoF system, all joints q_1, q_2, q_3, and q_4 are actuated.

Those experiments using ISFF used the linear proportional control law, as given in Eq. (18). The proportional gain $K_f \geq 0$ was related to the magnitude of the insertion force f_{ins}. K_f approaches zero as the insertion force f_{ins} increases up to a predetermined value $f_{\max}$. The values used for $V_{\max}$ and $V_{\min}$ were determined based on clinical observations and previous works [34].

$$V_{\text{ins}} = V_{\min} + K_f(V_{\max} - V_{\min}) \tag{18}$$

where

$$K_f = \begin{Bmatrix} (f_{\max} - f_{\text{ins}})/f_{\max} & f_{\text{ins}} \leq f_{\max} \\ 0 & f_{\text{ins}} > f_{\max} \end{Bmatrix}.$$

The parameters used are $f_{\max}=50$ g, $V_{\max}=2$ mm/s, and $V_{\min}$

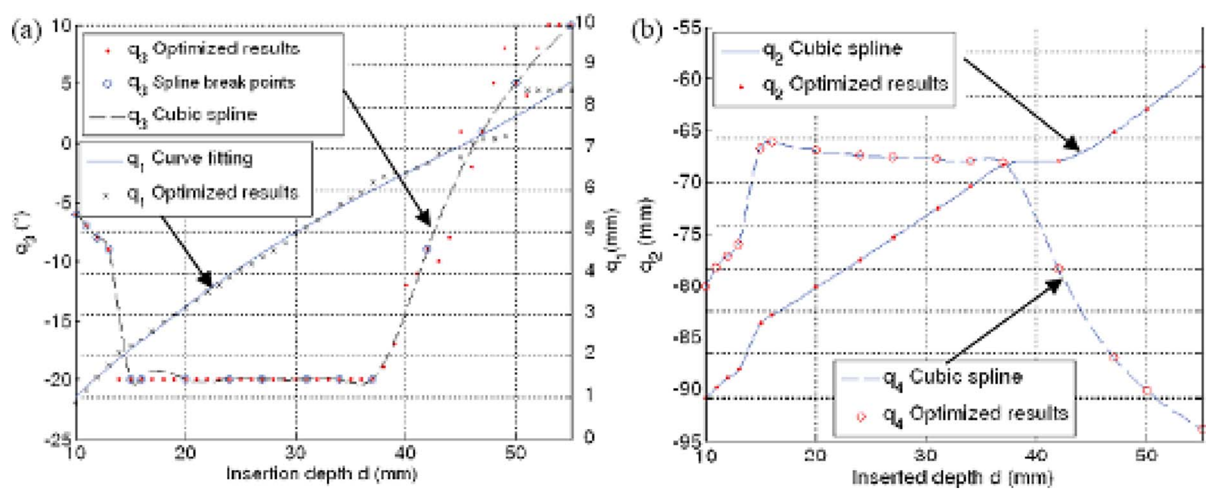

Fig. 8 Results for path planning: (*a*) bending of the electrode array q_1 and electrode array base rotation q_3 and (*b*) prismatic joint q_2 and prismatic joint q_4

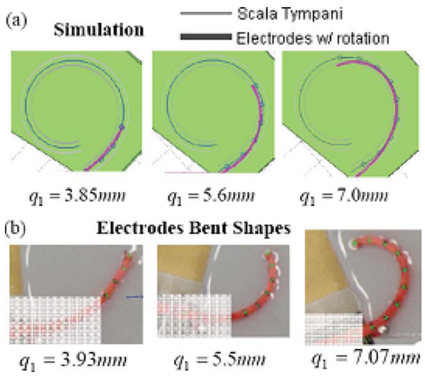

Fig. 10 Comparison of a simulated insertion with images taken during the electrode calibration: (*a*) simulation results for insertion based on (*b*) the calibrated model of the electrode

=0.22 mm/s.

Table 1 presents the experimental conditions tested using different experimental setups. In order to validate repeatability, the experiments were repeated three times for each experimental setup and insertion condition. In all cases, the same prototype electrode array, calibrated in Fig. 4, was used when comparing nonsteerable electrode array insertions with steerable insertions.

Figure 14 shows the insertion experimental results for each experimental condition given in Table 1. We note that those insertions using the nonsteerable electrode array into 3D scala tympani with ISFF failed to achieve full insertion due to buckling. This result is also shown in Figs. 16 and 17(*a*).

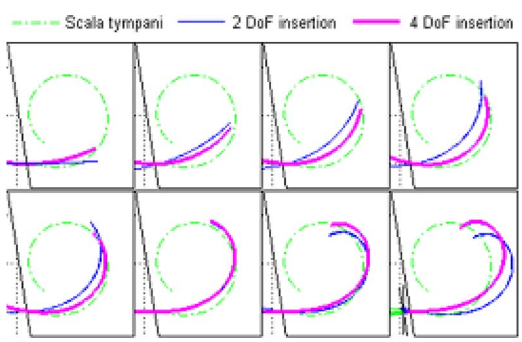

Fig. 11 Simulations for 2DoF insertion and 4DoF insertion

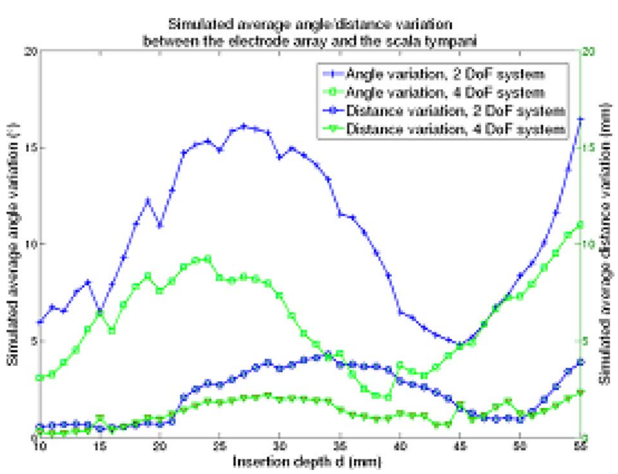

Fig. 12 Simulated average angle and distance variations

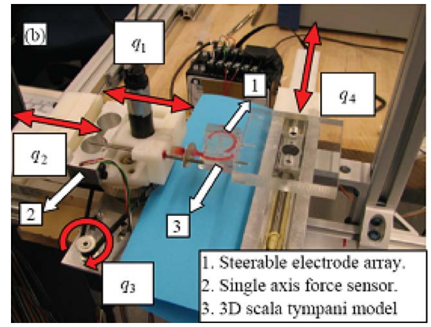

Fig. 13 System setup with 3D scala tympani model

6.2 Analysis of the Results of 1DoF and 2DoF Insertions

6.2.1 Steerable Versus Nonsteerable Electrode Array Insertions. Figure 15 shows the results of insertions into planar scalar tympani model. Comparing Fig. 15(*b*) with Fig. 15(*a*), the reduction in insertion force is obvious by using the steerable electrode array. The maximal insertion force is reduced by 59.6%. Comparing Fig. 15(*d*) with Fig. 15(*c*), using the steerable electrode reduces the maximal insertion force by 72.3%. All the groups in Fig. 15 use the planar scala tympani model, and the force impulse around $d=35$ mm is caused by the first contact between the tip of the electrode array and the outer wall of the scala tympani model. The same impulse force was observed in Fig. 18(*b*).

Figure 16 shows the insertion forces during insertions of the same nonsteerable electrode array into the 3D scala tympani model. For the nonsteerable electrode array, the insertion force is large enough to generate buckling of the electrode array. The encircled portion of the force readings in Fig. 16 shows the sudden

Table 1 Experimental conditions

	Insertion speed force feedback	2D scala tympani	3D scala tympani	Figure
1DoF setup		◆		15(*a*)
	◆	◆		15(*c*)
	◆		◆	16
2DoF setup		◆		15(*b*)
	◆	◆		15(*d*)
	◆		◆	16
4DoF setup		◆		18(*b*)
			◆	18(*a*)

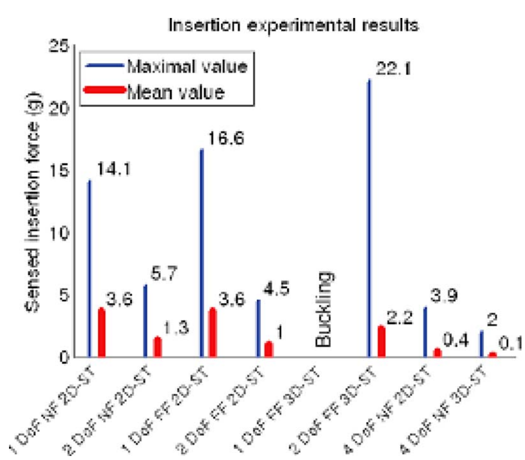

Fig. 14 Insertion results for average and maximal sensed forces for each experimental condition

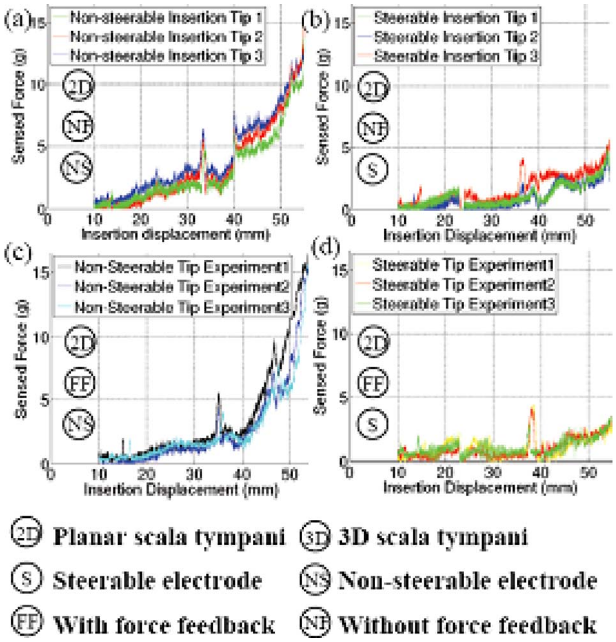

Fig. 15 Insertions using 2DoF system into planar scala tympani model: (*a*) nonsteerable electrode without ISFF, (*b*) steerable electrode without ISFF, (*c*) nonsteerable electrode with ISFF, and (*d*) steerable electrode with ISFF

decrease in the electrode stiffness due to buckling. This phenomenon is confirmed by the insertion video snapshots in Fig. 17(*a*). Using the steerable electrode array, the insertion can be achieved

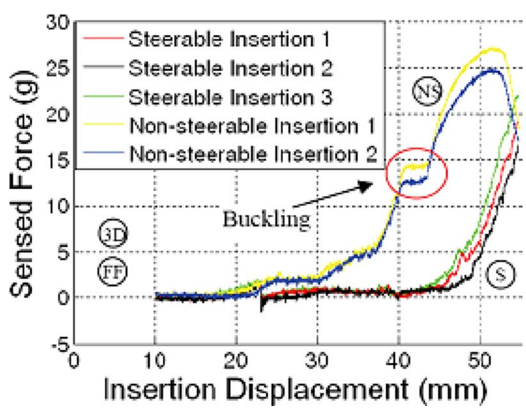

Fig. 16 Insertions using 2DoF system into 3D scala tympani model with ISFF for nonsteerable electrode array and steerable electrode array

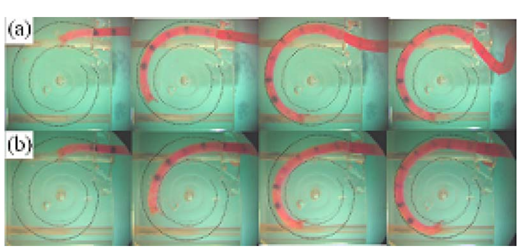

Fig. 17 Insertions using 2DoF system into 3D scala tympani model with ISFF: (*a*) nonsteerable electrode array, buckling happened and (*b*) steerable electrode array, no buckling happened

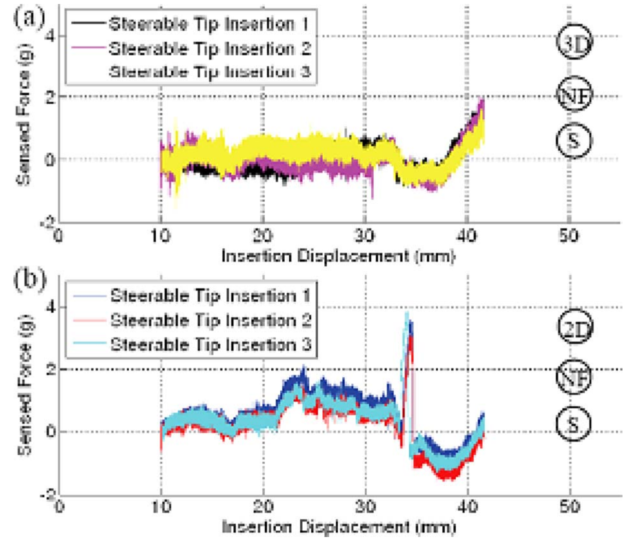

Fig. 18 Steerable electrode array insertions using 4DoF system without ISFF: (*a*) planar scala tympani model and (*b*) 3D scala tympani model

without buckling, as shown in Fig. 17(*b*).

In Fig. 16, the insertion force for the steerable electrode array increases quickly for insertions deeper than 45 mm because the geometric constraints of the scala tympani model do not allow further insertion of the electrode array. The planar scala tympani model does not present this problem because the model has a uniform cross section along the backbone curve of the scala tympani [5].

Due to the transparent property of the 3D scala tympani model, the boundaries of the scala tympani chamber are not very clear in Fig. 17. Hence, we emphasize the chamber boundaries by digitally highlighting the two boundary curves in Fig. 17.

6.2.2 Effect of ISFF. The results regarding the effect of ISFF are inconclusive. As seen from Fig. 14, comparing the insertion forces for nonsteerable insertions with and without ISFF (Figs. 15(*c*) and 15(*a*)), using the control law of Eq. (18) caused a 17.7% increase in the maximal insertion force while maintaining the same average insertion force. For 2DoF steerable insertions (Figs. 15(*d*) and 15(*b*)), using ISFF according to Eq. (18) reduced the insertion forces by 21.1% and 23.1% in maximal and average insertion forces, respectively. These results suggest that further research is needed to determine the optimal ISFF control law that replaces Eq. (18) and provides consistent results for steerable and nonsteerable electrode arrays. This control law depends on determining the correct friction model that takes into account viscous, stiction, and hydrodynamic effects.

6.3 Analysis of the Results of 4DoF Insertions. The second set of experiments was carried out using the 4DoF insertion system, Fig. 13, using the same steerable electrode array without ISFF. Figure 18 shows the results of inserting the steerable electrode array into the planar scala tympani model and the 3D scala tympani model. In both cases, the insertion forces are only 3.9 g and 2.0 g because of using the steerable electrode array.

For the 4DoF insertion system, the insertion is achieved up to 42 mm. Comparing Fig. 18(*b*) with Fig. 15(*b*), the maximal insertion force was reduced from 4.8 g to 3.9 g; 18.8% reduction was observed. Similarly, comparing Fig. 18(*a*) with Fig. 16, the maximal insertion forces up to 42 mm are comparable. However, we believe that as the insertions go deeper, using the 4DoF system will further decrease the insertion force compared with the 2DoF system.

In the case where the steerable electrode array was used (Figs.

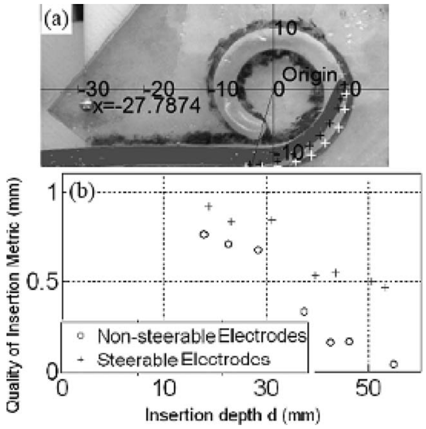

Fig. 19 (*a*) **Digitization of the average distance and** (*b*) **quality of insertion metric**

15(*b*), 15(*d*), 16, and 18), negative forces appeared when the steerable electrode array was steering and hugs the inner wall of the scala tympani model. Similar results are shown earlier in Ref. [34].

6.4 Quality of Insertion. For the experiments with the 2DoF system and the planar scala tympani model, Fig. 15, we digitized the edge of the scala tympani and the steerable electrode array for both nonsteerable and steerable electrode arrays, see Fig. 19(*a*). In the whole insertion process, seven pictures are digitized for each set.

We define the actual average distance between the electrode array and the scala tympani model as the quality of insertion metric, see Eq. (19).

$$\bar{p} = \frac{1}{d}\int_0^d \|\mathbf{r}_c(s) - \mathbf{r}_e(L-d+s)\| ds \tag{19}$$

where $\mathbf{r}_c(s)$ represents the actual point of the scala tympani at arclength s in $\{w\}$ and $\mathbf{r}_e(s)$ represents the actual point of the electrode array at arclength s in $\{w\}$.

As opposed to the simulated average angle and distance variations, which are defined in Eqs. (16) and (17), the quality of insertion metric describes the actual average distance between the electrode array and the scala tympani model during the insertion process. The quality of insertion metric is calculated and compared in Fig. 19(*b*) for both the nonsteerable and steerable electrode arrays. In both steerable and nonsteerable insertions, the actual average distance decreases as the insertion depth increases. However, the decrease rate is slower for the steerable electrode array than for the nonsteerable electrode array, implying that the steerable electrode array provides bigger gap between the electrode array and the scala tympani during the insertion process. Hence it explains the reduced insertion force when using the steerable electrode array [35].

7 Conclusion

This paper presented the clinical motivation and the optimal insertion path planning of the underactuated steerable electrode array for cochlear implant surgery. The problem of safely inserting a steerable electrode array into a 3D cavity (the scala tympani) was addressed using a novel steerable electrode array. The importance of steering the tip of the electrode array versus changing its approach angle with respect to the scala tympani was evaluated using simulations and experiments on both 2DoF and 4DoF robotic electrode insertion setups.

The path planning algorithm is based on minimizing the shape discrepancies of the bent electrode array and the scala tympani throughout all the insertion stages. A weighted optimization objective function was defined to balance shape discrepancies along the backbone of the inserted portion of the electrode array in order to minimize the required insertion forces. The closed-form solution to the calibration of the steerable electrodes was presented, and simulations of 2DoF insertions versus 4DoF insertions were carried out and evaluated using a theoretical insertion quality measure. This was verified experimentally on the planar and 3D models of the scala tympani.

The experiments presented in this work compared several insertion conditions including insertions into planar and 3D scala tympani models with or without steerable electrode arrays, with or without ISFF, and with or without changing the approach angle with respect to the scala tympani (2DoF insertion setup versus 4DoF insertion setup).

The experimental results show that steerable insertions significantly reduced insertion forces than nonsteerable insertions. The effects of applying ISFF control to minimize the insertion force for steerable and nonsteerable electrode arrays are not consistent. A potential optimization of the ISFF control law needs further investigation. It was also shown that the added freedoms of the 4DoF insertion system reduced the required insertion forces compared with the 2DoF insertion system.

We believe that these experiments provide a justification for pursuing robot-assisted insertion of steerable electrode array for cochlear implant surgery. Future work will include miniaturization

Table 2 Spline coefficients for q_2^*, q_3^*, and q_4^*

	q_2^*				q_3^*				q_4^*			
j	$b_{j,4}\times 10^{-2}$	$b_{j,3}\times 10^{-2}$	$b_{j,2}\times 10^{-2}$	$b_{j,1}$	$b_{j,4}\times 10^{-2}$	$b_{j,3}\times 10^{-2}$	$b_{j,2}\times 10^{-2}$	$b_{j,1}$	$b_{j,4}\times 10^{-2}$	$b_{j,3}\times 10^{-2}$	$b_{j,2}\times 10^{-2}$	$b_{j,1}$
1	−7.334	19.861	80.431	−90.87	31.398	−94.193	−37.205	−6	−8.412	−24.233	268.83	−2.27
2	−7.334	−2.143	98.15	−89.94	31.398	2.22×10^{-14}	−131.4	−7	−8.412	−49.47	195.13	0.088
3	43.164	−24.146	71.862	−89.06	−156.99	94.193	−37.205	−8	137.96	−74.706	70.954	1.460
4	−35.51	105.35	153.06	−88.15	130.83	−376.77	−319.78	−9	−114.9	339.19	335.43	2.802
5	38.554	−107.71	148.32	−83.71	−151.32	408.21	−256.89	−20	117.51	−350.24	313.32	13.89
6	−0.814	7.9472	48.555	−82.92	4.8386	−45.748	105.57	−20	−0.042	2.285	−34.637	14.69
7	0.2022	−1.826	73.042	−80.23	−1.319	12.316	−28.155	−20	−0.114	1.7839	−18.361	13.65
8	−0.042	0.6003	68.142	−77.47	0.3883	−3.515	7.0488	−20	0.0943	0.4172	−9.556	13.12
9	−0.091	0.218	70.597	−75.38	0.2271	−0.02	−3.554	−20	−0.39	1.2658	−4.507	12.9
10	0.5555	−0.88	67.949	−72.58	−1.7	2.7052	7.1876	−20	1.8441	−3.416	−13.109	12.67
11	−2.191	4.1199	77.669	−70.47	6.6983	−12.598	−22.491	−20	−7.187	13.181	16.184	12.47
12	1.7469	−15.598	43.236	−68.36	−4.048	47.687	82.776	−20	4.4842	−51.505	−98.79	12.20
13	−0.666	10.605	18.275	−67.92	0.3673	−13.039	256.01	−9	−0.422	15.757	−277.53	−0.01
14	6.25×10^{-3}	0.6204	74.403	−65.19	0.306	−7.529	153.17	1	−0.405	9.4338	−151.57	−10.47
15	6.25×10^{-3}	0.6767	78.294	−62.90	0.306	−4.778	116.25	5	−0.405	5.789	−105.91	−14.28

of the steerable electrode arrays, elastic modeling and simulation-based calibration of these electrodes, and insertion experiments on human cadaver cochlea.

Acknowledgment

This work was supported by National Science Foundation (NSF) Grant No. 0651649. The authors thank Elizabeth Olson from Columbia University for providing references for dimensioning the cross sections of the scala tympani.

Appendix

Spline coefficients for q_2^*, q_3^*, and q_4^* are shown in Table 2.

References

[1] Jayender, J., Patel, R. V., and Nikumb, S., 2006, "Robot-Assisted Catheter Insertion Using Hybrid Impedance Control," *Proceedings of the IEEE International Conference on Robotics and Automation*, pp. 607–612.
[2] Ikuta, K., Ikuta, K., Yamamoto, K., and Sasaki, K., 2003, "Development of Remote Microsurgery Robot and New Surgical Procedure for Deep and Narrow Space," *Proceedings of the IEEE International Conference on Robotics and Automation*, Vol. 1, pp. 1103–1108.
[3] Chang, J. K., Chung, S., Lee, Y., Park, J., Lee, S. K., Yang, S. S., Moon, S. Y., Tschepe, J., Chee, Y., and Han, D. C., 2002, "Development of Endovascular Microtools," J. Micromech. Microeng., **12**(6), pp. 824–831.
[4] Dario, P., Carrozza, M. C., and Pietrabissa, A., 1999, "Development and In Vitro Testing of a Miniature Robotic System for Computer-Assisted Colonoscopy," Comput. Aided Surg., **4**(1), pp. 1–14.
[5] Zhang, J., Xu, K., Simaan, N., and Manolidis, S., 2006, "A Pilot Study of Robot-Assisted Cochlear Implant Surgery Using Steerable Electrode Arrays," *Medical Image Computing and Computer-Assisted Intervention* (Lecture Notes in Computer Science Vol. 4190), Springer Berlin/Heidelberg, Copenhagen, Denmark, pp. 33–40.
[6] Zheng, Y. F., Pei, R., and Chen, C., 1991, "Strategies for Automatic Assembly of Deformable Objects," *Proceedings of the IEEE International Conference on Robotics and Automation*, Vol. 3, pp. 2598–2603.
[7] Rohde, F. V., 1953, "Large Deflections of Cantilever Beam With Uniformly Distributed Load," Q. Appl. Math., **11**, pp. 337–338.
[8] Nakagaki, H., Kitagi, K., Ogasawara, T., and Tsukune, H., 1996, "Study of Insertion Task of a Flexible Wire Into a Hole by Using Visual Tracking Observed by Stereo Vision," *Proceedings of the IEEE International Conference on Robotics and Automation*, Vol. 4, pp. 3209–3214.
[9] Wakamatsu, H., Hirai, S., and Iwata, K., 1996, "Static Analysis of Deformable Object Grasping Based on Bounded Force Closure," *Proceedings of the IEEE International Conference on Robotics and Automation*, Vol. 4, pp. 3324–3329.
[10] Liu, Z., and Nakamura, T., 2002, "Learning Insertion Task of a Flexible Beam by Virtual Agents," *Proceedings of the IEEE International Conference on Robotics and Automation*, Vol. 3, pp. 3290–3295.
[11] Suzumori, K., Iikura, S., and Tanaka, H., 1992, "Applying a Flexible Microactuator to Robotic Mechanisms," IEEE Control Syst. Mag., **12**(1), pp. 21–27.
[12] Nakagaki, H., Kitagaki, K., and Tsukune, H., 1995, "Study of Insertion Task of a Flexible Beam Into a Hole," *Proceedings of the IEEE International Conference on Robotics and Automation*, Vol. 1, pp. 330–335.
[13] Chirikjian, G. S., and Burdick, J. W., 1994, "A Modal Approach to Hyper-Redundant Manipulator Kinematics," IEEE Trans. Rob. Autom., **10**(3), pp. 343–354.
[14] Zanganeh, K. E., and Angeles, J., 1995, "The Inverse Kinematics of Hyper-Redundant Manipulators Using Splines," *Proceedings of the IEEE International Conference on Robotics and Automation*, Vol. 3, pp. 2797–2802.
[15] Mochiyama, H., and Kobayashi, H., 1999, "The Shape Jacobian of a Manipulator With Hyper Degrees of Freedom," *Proceedings of the IEEE International Conference on Robotics and Automation*, Vol. 4, pp. 2837–2842.
[16] Kiefer, J., Weber, A., Pfennigdorff, T., and Von Ilberg, C., 2000, "Scala Vestibuli Insertion in Cochlear Implantation: A Valuable Alternative for Cases With Obstructed Scala Tympani," ORL, **62**(5), pp. 251–256.
[17] Roland, J. T. J., 2005, "A Model for Cochlear Implant Electrode Insertion and Force Evaluation: Results With a New Electrode Design and Insertion Technique," Laryngoscope, **115**(8), pp. 1325–1339.
[18] Kha, H. N., Chen, B. K., Clark, G. M., and Jones, R., 2004, "Stiffness Properties for Nucleus Standard Straight and Contour Electrode Arrays," Med. Eng. Phys., **26**(8), pp. 677–685.
[19] Patrick, J., and McFarlane, J., 1987, "Characterization of Mechanical Properties of Single Electrodes and Multielectrodes," Ann. Otol. Rhinol. Laryngol., **96**, pp. 46–48.
[20] Chen, B. K., Clark, G. M., and Jones, R., 2003, "Evaluation of Trajectories and Contact Pressures for the Straight Nucleus Cochlear Implant Electrode Array—A Two Dimensional Application of Finite Element Analysis," Med. Eng. Phys., **25**, pp. 141–147.
[21] Wardrop, P., Whinney, D., Rebscher, S. J., Roland, J. J. T., Luxford, W., and Leake, P. A., 2005, "A Temporal Bone Study of Insertion Trauma and Intracochlear Position of Cochlear Implant Electrodes. I: Comparison of Nucleus Banded and Nucleus Contour™ Electrodes," Hear. Res., **203**(1–2), pp. 54–67.
[22] Adunka, O., Gstoettner, W., Hambek, M., Unkelbach, M. H., Radeloff, A., and Kiefer, J., 2004, "Preservation of Basal Inner Ear Structures in Cochlear Implantation," ORL, **66**(6), pp. 306–312.
[23] Adunka, O., Kiefer, J., Unkelbach, M. H., Lehnert, T., and Gstoettner, W., 2004, "Development and Evaluation of an Improved Cochlear Implant Electrode Design for Electric Acoustic Stimulation," Laryngoscope, **114**(7), pp. 1237–1241.
[24] Eshraghi, A. A., Yang, N. W., and Balkany, T. J., 2003, "Comparative Study of Cochlear Damage With Three Perimodiolar Electrode Designs," Laryngoscope, **113**(3), pp. 415–419.
[25] Chen, B., Kha, H., and Clark, G., 2007, "Development of a Steerable Cochlear Implant Electrode Array," Third Kuala Lumpur International Conference on Biomedical Engineering, pp. 607–610.
[26] Wang, J., Gulari, M. N., and Wise, K. D., 2006, "A Parylene-Silicon Cochlear Electrode Array With Integrated Position Sensors," 28th Annual International Conference of the IEEE—Engineering in Medicine and Biology Society, pp. 3170–3173.
[27] Cohen, L., Xu, J., Xu, S. A., and Clark, G. M., 1996, "Improved and Simplified Methods for Specifying Positions of the Electrode Bands of a Cochlear Implant Array," Am. J. Otol., **17**, pp. 859–865.
[28] Yoo, S. K., Wang, G., Rubinstein, J. T., Skinner, M. W., and Vannier, M. W., 2000, "Three-Dimensional Modeling and Visualization of the Cochlea on the Internet," IEEE Trans. Inf. Technol. Biomed., **4**(2), pp. 144–151.
[29] Ketten, D. R., Skinner, M. W., Wang, G., Vannier, M. W., Gates, G. A., and Neely, J. G., 1998, "In Vivo Measures of Cochlear Length and Insertion Depth of Nucleus Cochlear Implant Electrode Arrays," Ann. Otol. Rhinol. Laryngol., **107**(175), pp. 1–16.
[30] Wysocki, J., 1999, "Dimensions of the Human Vestibular and Tympanic Scalae," Hear. Res., **135**(1–2), pp. 39–46.
[31] Angeles, J., and Lopez-Cajun, C., 1991, *Optimization of Cam Mechanisms*, Kluwer Academic, Dordrecht.
[32] Graham, A., 1981, *Kronecker Products and Matrix Calculus With Applications* (Ellis Horwood Series: Mathematics and Its Applications), Ellis Horwood Limited, New York.
[33] Rogers, D. F., and Adams, A. J., 1990, *Elements for Computer Graphics*, 2nd ed., McGraw-Hill, New York.
[34] Todd, C. A., Naghdy, F., and Svehla, M. J., 2007, "Force Application During Cochlear Implant Insertion: An Analysis for Improvement of Surgeon Technique," IEEE Trans. Biomed. Eng., **54**(7), pp. 1247–1255.
[35] Juvinall, R., and Marshek, K., 2003, *Fundamentals of Machine Component Design*, Wiley, New York.